Check for updates

Advanced Engineering Materials

ADVANCED ENGINEERING MATERIALS
www.aem-journal.com

RESEARCH ARTICLE OPEN ACCESS

High-Temperature Nanoindentation of Metals: Assessing Thermal Drift, Frame Compliance, and Chemical Composition Effects on the Reported Mechanical Properties

Velislava Yonkova[1] | Steffen Brinckmann[1] | Ruth Schwaiger[1,2]

[1]Forschungszentrum Jülich GmbH, Institute of Energy Materials and Devices, Structure and Function of Materials (IMD-1), Jülich, Germany | [2]Chair of Energy Engineering Materials, Faculty 5, RWTH Aachen University, Aachen, Germany

Correspondence: Steffen Brinckmann (s.brinckmann@fz-juelich.de)

Received: 18 December 2025 | **Revised:** 24 February 2026 | **Accepted:** 26 February 2026

Keywords: experimental artifacts | high temperature | nanoindentation

ABSTRACT

High-temperature nanoindentation measurements are compromised by instrument-related artifacts, such as thermal drift and temperature-dependent apparent frame compliance. In this study, we quantify the influence of these artifacts on apparent mechanical properties by comparing static nanoindentation across temperatures and by analyzing the resulting data with two processing routes: the classical Oliver–Pharr method and an automatic image recognition (AIR) method. Significant thermal drift was observed at elevated temperatures and was found to alter the apparent frame compliance and contact-depth determination. Both analysis methods show a systematic reduction in hardness with increasing temperature. Multiple ferritic, martensitic, and austenitic steels as well as a Ni-based alloy were examined to probe the compositional and microstructural contributions to thermal stability. Despite substantial scatter inherent to elevated-temperature testing, statistical analysis indicates that Cr and Ni additions improve resistance to softening. Combining Oliver–Pharr and AIR analyses enables more reliable extraction of mechanical properties related to the alloy composition at elevated temperatures when instrument artifacts are explicitly considered.

1 | Introduction

Nanoindentation is a widely used technique for probing micromechanical properties at localized length scales, enabling quantification of microstructural effects (e.g., grain orientation, phase distributions, and inclusions) that cannot be resolved by conventional bulk tensile or compression testing. It is routinely employed to determine hardness, Young's modulus, creep behavior, and fracture toughness of heterogeneous materials [1, 2]. While hardness typically exhibits strong temperature dependence, Young's modulus is generally less sensitive. Accurate high-temperature measurements are essential for understanding these materials' properties and the material performance under service conditions [3].

The Oliver–Pharr (O–P) method [1] is the most widely applied protocol for determining hardness and elastic modulus from instrumented indentation data across engineering and scientific disciplines [4]. In a standard nanoindentation test, a normal force is monotonically applied to a specimen surface via a hard, stiff indenter (typically a pyramidal or spherical diamond or carbide tip) and then removed to zero force. The resulting force–displacement response is analyzed, and the unloading stiffness, peak force, and corresponding penetration depth are used to determine contact area, hardness, and elastic modulus [1]. High-temperature nanoindentation introduces additional experimental complexities, including sample mounting, elevated tip wear, precise and stable temperature control, and instrument stability. Review articles and experimental studies have highlighted

This is an open access article under the terms of the Creative Commons Attribution License, which permits use, distribution and reproduction in any medium, provided the original work is properly cited.

© 2026 The Author(s). *Advanced Engineering Materials* published by Wiley-VCH GmbH.

recurrent issues such as thermal drift, oxidation and other high-temperature surface reactions, contamination, and the need for high-temperature calibration procedures [3, 5–8]. Wheeler et al. [3] emphasized the importance of improved heater designs and low-noise power supplies to achieve thermally stable testing conditions. A key technical limitation is the identification of indenter materials that maintain mechanical integrity and chemical inertness at elevated temperatures; Wheeler et al. [9] demonstrated that common candidate materials (e.g., alumina, tungsten carbide, and cubic boron nitride) exhibit markedly different degrees of thermal stability and wear behavior. Beake and Smith [5] studied fused silica deformation at elevated temperature as a potential calibration standard and concluded that it is suitable only at ambient conditions, as its apparent modulus increases with temperature, compromising its use for high-temperature calibration. Additional challenges have been highlighted by Schuh and co-workers [6, 8], including discrepancies in temperature calibration between indenter tip and specimen, the need for meticulous surface preparation, and diamond tip degradation at temperatures near 500°C. Although thermal drift rates below 1 nm/s have been reported up to 400°C, maintaining such low drift while preventing tip and sample degradation remains challenging. Verma et al. [10] focused on reducing drift prior to testing. Schmahl et al. [11], however, found that pre-experimentation drift quantification and linear drift extrapolation are insufficient. They measured the drift of a piezo-based stage on a number of materials and used these values as references for subsequent measurements, without investigating other potential drift influences. Collectively, precise temperature control, indenter tip stability, and minimization and quantification of thermal drift constitute the primary obstacles to reliable high-temperature nanoindentation.

To address instrument-related drift, researchers have developed alternative setups, most notably systems with dual measurements heads. Nohava et al. [12] introduced a nanoindentation system with active top referencing to minimize thermal drift and ensure long-term measurement stability. Conte et al. [13] reported a high-temperature nanoindenter employing active surface referencing, independent heating of indenter and specimen, and vacuum conditions, achieving minimized thermal drift (<2 nm/min). However, these systems require substantial modifications to nanoindentation instruments, limiting their universal applicability.

This study examined metals spanning a range of crystal structures (ferritic, martensitic, austenitic, and a Ni-based face-centered-cubic (FCC) alloy) and a broad spectrum of chromium and nickel concentrations. These selections were made to address two coupled questions. First, how do measurement artifacts arising at elevated temperature—such as thermal drift, apparent frame compliance changes, and creep—affect standard indentation metrics across different alloy classes? Second, can meaningful composition–property trends (e.g., the roles of Cr and Ni in solid-solution and precipitation strengthening, and their influence on high-temperature stability) be extracted in the presence of such instrumental artifacts? To address these questions, we combine the O–P analysis (which is sensitive to depth-based artifacts) with an image-based automatic image recognition (AIR) [14] approach that directly measures the residual contact area, together with statistical evaluation. This integrated strategy is designed to disentangle instrument-related variability from genuine material trends associated with chemistry and microstructure. Accordingly, the composition-focused analysis presented here is exploratory in nature: it asks whether statistically meaningful composition–property correlations can be recovered after explicit treatment of instrumental artifacts, within the inherent limitations of high-temperature nanoindentation.

We investigate the temperature range from ambient to service temperatures (20°C–600°C) relevant to steam-power and petrochemical systems, which typically operate from several tens to several hundreds degrees and up to approximately 600°C or higher. Within this temperature window, thermally activated processes (such as recovery, the onset of creep, solute redistribution, precipitate evolution, and oxidation) can progressively influence the local mechanical response.

2 | Materials and Methods

2.1 | Materials

We selected seven different alloys with varied Cr and Ni contents to assess the thermal stability of their mechanical properties. The alloys were deliberately selected to (i) cover a broad, industry-relevant range of Cr and Ni contents (from low-alloy ferritic steels up to high-Ni alloys), and (ii) represent the main structural and crystallographic classes used in high-temperature engineering (including ferritic, martensitic, austenitic steels, as well as a Ni-based superalloy). This selection enables investigation of how Cr and Ni, and their associated microstructural families affect hardness and thermal stability, while also revealing how measurement artifacts develop under practical service temperatures.

One specimen was prepared from each alloy and the bulk chemical compositions were quantified by inductively coupled plasma optical emission spectroscopy (ICP-OES) and infrared (IR) spectroscopy (see Table 1). Specimens measuring $0.5 \times 0.5\ \mathrm{cm}^2$ with a thickness of approximately 1 mm were mechanically ground and polished with SiC paper and different diamond suspensions. The final polishing was conducted using an oxide polishing suspension (OPS), resulting in an average surface roughness of $R_a = 6 - 24$ nm for the different metals as determined by the Olympus LEXT OLS4000, as detailed in Section 2.3. Subsequently, the specimens were mounted on the nanoindentation sample holder using a high-temperature cement (OMEGABOND OB-600).

2.2 | Nanoindentation Experiments

Nanoindentation experiments were performed using a NanoTest Xtreme (Micromaterials Ltd., Wrexham, UK) equipped with a cubic boron nitride (cBN) Berkovich indenter tip. The indenter tip material (cubic boron nitride) was selected for its superior thermal and chemical stability compared with diamond in oxidizing and high-temperature environments (see Wheeler et al. [3, 15]), supporting the assumption of a temperature-stable tip geometry over the investigated temperature range. Nevertheless, temperature-dependent tip deformation, wear, or chemical interactions cannot be entirely excluded and may introduce additional uncertainty into depth-based O–P quantities. To mitigate sensitivity to this potential bias, we (i) report AIR-derived hardness values, which do not rely on the calibrated tip area function, and (ii) focus on trends that remain consistent across both O–P and AIR analyses.

Tests were carried out in a low-pressure nitrogen environment ($1 \cdot 14;10^{-5}$ mbar) to minimize oxidation. Indentations were conducted at four temperatures: 20°C, 200°C, 400°C, and 600°C.

15272648, 0, Downloaded from https://advanced.onlinelibrary.wiley.com/doi/10.1002/adem.202503193 by Universitatsbibliothek RWTH Aachen University, Wiley Online Library on [23/04/2026]. See the Terms and Conditions (https://onlinelibrary.wiley.com/terms-and-conditions) on Wiley Online Library for rules of use; OA articles are governed by the applicable Creative Commons License

TABLE 1 | Chemical composition of the alloys investigated determined by ICP-OES and IR spectroscopy. Crystal structures (cs) are taken from the respective manufacturer datasheets. Values are reported as elemental concentrations in wt%.

cs	Ferritic			Martensitic	Austenitic		FCC
Alloy	**16Mo3**	**13CrMo4-5**	**10CrMo9-10**	**X10CrMoVNb9-1**	**X6CrNi18-10**	**X1NiCrMoCuN31-27-4**	**NiCr23Co12M**
name				T91	DMV 304HCu	Sanicro 25	Alloy 617
Fe	97.8	96.1	96.2	88.8	68.8	41.9	0.466
C	0.1433	0.1559	0.1056	0.1207	0.087	0.0646	0.0577
Cr	0.11	1.04	2	8.9	18.7	22.6	20.3
W	—	0.000408	0.000745	—	—	3.7	0.0096
V	—	0.0067	0.0064	0.22	—	—	0.00613
Si	0.24	0.29	0.298	0.32	0.2	0.15	0.541
P	0.01	0.0192	0.0206	0.014	0.012	0.015	<0.004
Ni	0.094	0.0621	0.0459	0.26	8.7	25.4	55.5
Nb	—	<0.002	<0.002	0.078	0.43	0.48	0.0062
Mo	0.25	0.423	0.982	0.94	—	—	9.3
Mn	0.59	0.566	0.57	0.45	0.75	0.5	0.0158
Cu	0.096	0.2035	0.0257	0.11	2.8	2.9	0.0614
Co	—	0.01078	0.0069	—	—	1.5	11.9
B	—	0.0172	0.0175	—	—	—	<0.006
Al	0.022	0.02701	0.0325	0.014	0.016	0.062	0.84
N	0.0061	0.0036	0.0064	0.0577	0.1106	0.2317	0.0235
S	0.0086	0.0023	0.0038	<0.0005	<0.0005	<0.0005	0.0015
Ti	—	0.00217	0.0017	—	—	—	0.355
O	0.0226	0.0029	0.0033	0.0549	0.0366	0.0165	<0.0014

Heating was applied at 10 K/min, with isothermal stabilization periods of 1 h upon reaching 200°C and 400°C. For the 600°C experiments, the temperature was increased from 200°C, and the stabilization period was extended to 2 h. Both single loading–unloading and cyclic loading–unloading protocols were used (Figure 1). The indenter area function was determined via cyclic loading–unloading calibration on fused silica at 20°C using nine indentations with 20 loading–unloading cycles each and was assumed to be independent of temperature. It should be noted that fused silica changes its properties with temperature [16] and cannot be used as a calibration material at elevated temperatures.

Single-cycle (full unload) and cyclic (multicycle, partial-unload) indentation protocols were performed. The cyclic protocol constitutes the primary dataset and underpins the

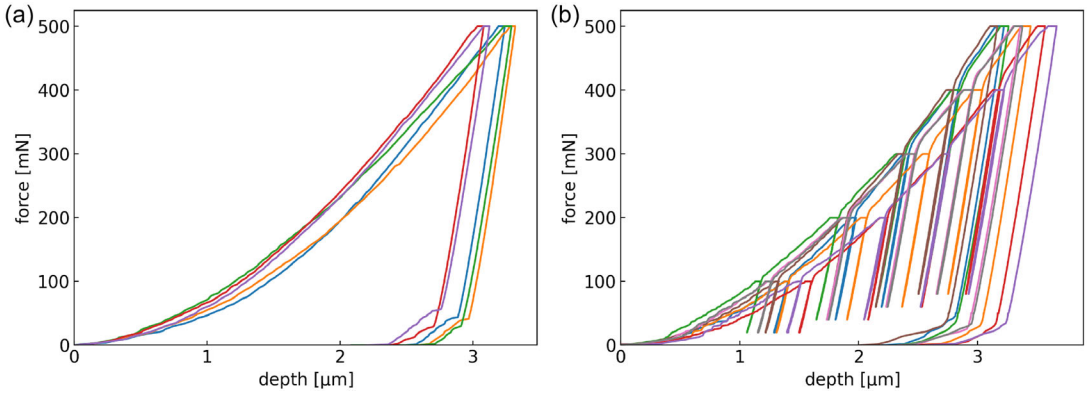


FIGURE 1 | Representative force–depth curves measured on 13CrMo4-5 (see Table 1) at 20°C. (a) Single loading–unloading cycle to a peak force of 500 mN (15 s loading, 5 s hold). (b) Cyclic loading–unloading sequence consisting of five cycles to a peak force of 500 mN (5 s loading and 5 s hold per cycle). Both indentation protocols were employed in this study. The cyclic (multicycle, partial-unload) protocol provides the primary dataset for frame-compliance calibration, drift, and creep analysis, and for the O–P versus AIR comparisons reported in the main results. The single-cycle measurements serve as a secondary comparison to demonstrate the effects of omitting sample-specific frame-compliance calibration.

15272648, 0, Downloaded from https://advanced.onlinelibrary.wiley.com/doi/10.1002/adem.202503193 by Universitatsbibliothek RWTH Aachen University, Wiley Online Library on [23/04/2026]. See the Terms and Conditions (https://onlinelibrary.wiley.com/terms-and-conditions) on Wiley Online Library for rules of use; OA articles are governed by the applicable Creative Commons License

frame-compliance calibration, explicit quantification of thermal drift and creep corrections, and the comparative O–P versus AIR analyses presented in the main results. In contrast, single-cycle measurements were performed in two independent test series and serve as a secondary comparison, illustrating the consequences of omitting sample-specific frame-compliance calibration and explicit drift quantification.

Single loading–unloading tests were carried out to a peak force of 500 mN, with 15 s loading and unloading segments and a 5 s hold at peak force, using a linear force ramp. The seven materials listed in (Table 1) were tested in two campaigns: set 1 included the ferritic and martensitic specimens, while set 2 included the remaining alloys. The T91 specimen was included in both sets to enable direct comparison. These experiments employed the frame stiffness obtained from the fused silica calibration and omitted thermal drift quantification.

Cyclic loading–unloading tests, although more time-consuming, enable frame-compliance calibration. At elevated temperatures, this approach is particularly challenging because prolonged test durations increase time-dependent creep and instrumental drift. To maintain consistent testing conditions, all seven specimens were mounted on a single holder and characterized during one continuous test campaign. A limitation of this arrangement is thermal nonuniformity: specimens near the periphery of the holder may experience slightly different temperatures than those at the center, potentially introducing systematic variation.

Cyclic indentation consisted of five loading–unloading cycles performed at a constant loading rate to a maximum force of 500 mN. Successive cycles reached peak forces of 100, 200, 300, 400, and 500 mN. Each cycle included a 5 s loading, 5 s holding at peak force, and 5 s unloading. The first four cycles were unloaded to 20% of the respective peak force; the final cycle was unloaded to 10% (i.e., to 50 mN).

2.3 | Calibrations and Data Analysis

This study focuses on the temperature-induced artifacts, particularly thermal drift. Drift was quantified after unloading to 10% of the peak force and holding the residual force for 15 s. During this period, indenter displacement was continuously recorded, and a linear least-squares fit was applied to the depth-time data; the slope of this fit was taken as the drift rate. Drift correction was performed by back-extrapolating this linear drift, i.e., multiplying the drift rate by elapsed time and subtracting the result from the measured depth. This correction was applied prior to the compliance correction described below.

The loading configuration (penetration depth h, peak normal force p, and contact compliance C_c) is required when determining the contact mechanical properties (contact area A_c and reduced modulus E_r), according to Sneddon-like theories [17, 18]. The contact compliance depends on the measured compliance $C_{measured}$ and frame compliance C_{frame}, the latter was calibrated for each specimen individually using the cyclic loading protocol to account for variability introduced by the high-temperature cement and the specimen's position on the holder. Hence, $C_{measured}$ can be written as

$$C_{measured} = C_{frame} + C_c = C_{frame} + \sqrt{\frac{\pi}{4A_cE_r^2}} = C_{frame} + \frac{\sqrt{\pi H}}{2E_r}\frac{1}{\sqrt{p}} = C_{frame} + m\frac{1}{\sqrt{p}} \quad (1)$$

where m is the fitted slope. The intercept of the compliance in Figure 2 corresponds to the frame compliance, which is subtracted from $C_{measured}$ to yield C_c [14]. The uncertainty in the frame compliance was determined from the standard deviation of the fitted intercept using the NumPy library (v1.26) [19]. A linear regression yielded the covariance matrix (whose diagonal entries correspond to the parameter variances). The relative error (in percent) was then calculated as $100\sqrt{\sigma_{dev}}/C_{frame}$, where σ_{dev} is the variance associated with the fitted frame compliance C_{frame}.

The actual geometry of an indenter tip—and thus its contact area—deviates from the idealized shape. Accordingly, the true tip shape is determined experimentally by performing indents on a reference material (here, fused silica) and using its known elastic modulus to determine the contact area as a function of penetration depth. This area-function calibration procedure is well established and described in detail elsewhere [18].

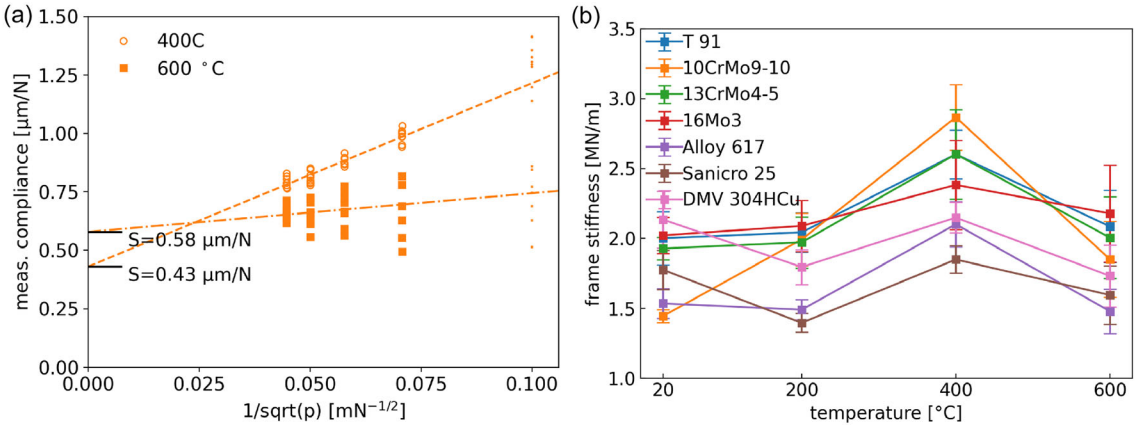


FIGURE 2 | (a) Frame compliance calibrations from cyclic loading measurements at 400°C and 600°C on 10CrMo9-10. The data points at the right-hand side are excluded as the represent normal forces less than 150 mN, i.e., assumed imperfectly established contact of tip–sample. (b) Frame stiffness, i.e., inverse of frame compliance, as a function of temperature for all samples. The frame stiffness is approximately 2 MN/m.

15272648, 0, Downloaded from https://advanced.onlinelibrary.wiley.com/doi/10.1002/adem.202503193 by Universitatsbibliothek RWTH Aachen University, Wiley Online Library on [23/04/2026]. See the Terms and Conditions (https://onlinelibrary.wiley.com/terms-and-conditions) on Wiley Online Library for rules of use; OA articles are governed by the applicable Creative Commons License

Indentation data for the seven materials investigated were analyzed using two complementary approaches as shown in Figure 3: the O–P method [1]—the standard benchmark for nanoindentation analysis, and an AIR algorithm [14]. Because the O–P framework is widely documented, a full description is omitted here; emphasis is placed instead on the AIR implementation, see below, and on any relevant departures from the standard O–P analysis, see next paragraph.

Measurements at 20°C, 200°C, and 400°C did not reveal time-dependent (creep) deformation because the penetration depth decreased immediately upon unloading during the nanoindentation experiment. The conventional O–P analysis was used for these tests. However, to account for creep at 600°C, the elastic modulus measured at this temperature was corrected following the procedure of Ngan et al. [20]. Their method adjusts the apparent contact stiffness, S, to obtain a corrected stiffness, S_e, which is then used to calculate the viscoelastic-corrected elastic modulus:

$$\frac{1}{S_e} = \frac{1}{S} - \frac{\dot{h}_h}{\dot{P}_u} \tag{2}$$

Here, S denotes the apparent contact stiffness obtained using the O–P method. The term $\dot{h}_h$ is the displacement rate, computed via the NumPy `gradient` function [19] applied to the depth signal over the final second prior to unloading, and $\dot{P}_u$ is the prescribed unloading rate. The corrected stiffness S_e is then substituted into the O–P expression for the reduced modulus to obtain the viscoelastic-corrected elastic modulus.

Indentation imprints were characterized using the AIR method following cyclic loading–unloading nanoindentation tests. Surface topography was acquired with an Olympus LEXT OLS4000 3D Laser Measuring Microscope at 100× magnification, producing a stitched three-dimensional map of the indentation pattern. Stitch seams were intentionally positioned to avoid intersecting any imprints, thereby minimizing stitching artifacts during contour detection. The raw datasets, consisting of both height and light-intensity channels, were processed in Gwyddion [21] to level the topography, exported as ASCII (.txt) files, and subsequently analyzed using a custom Python script. Only the height channel was used for analysis. Each indentation imprint was analyzed using a stepwise algorithm (Figure 4):

1. Deepest-point localization: the deepest point within each imprint was identified and its coordinates and height were stored in a Python list.
2. Thresholding and contour detection:
   a. Fifty threshold levels between 1 and 10 µm were applied (with a step size of 0.18 µm).
   b. For each threshold, a binary image was generated in which pixels with elevations below the threshold were assigned to the foreground.
   c. Contours were detected in each binary image using `findContours` function in OpenCV v4.8.1 [22].
   d. For each threshold, the contour enclosing the previously identified deepest point was selected for further analysis (see Figure 4)).
   e. To eliminate spurious detections, contours with areas smaller than 1000 pixels or larger than 8% of the imprint section area were discarded.
3. Determination of the optimal threshold and contact area:
   a. The numerical derivative of the contour area with respect to the threshold (area gradient) was computed using NumPy's `gradient` function.
   b. At low threshold values, the area gradient remained zero because detected contours did not meet the minimum area criterion. As the threshold increased, the contour area—and consequently the area gradient—increased until the physical edge of the imprint was exceeded.
   c. Beyond this point, the contour flooded the image, exceeded the maximum area criterion, and produced a negative change in the area gradient.
   d. The optimal threshold was defined as the first threshold at which the area gradient became negative,

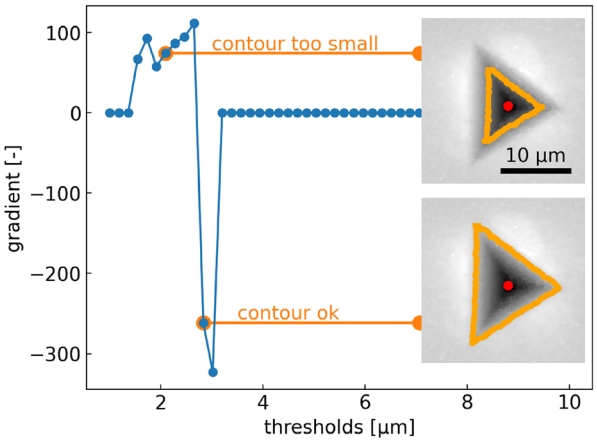


FIGURE 4 | Determination of the optimal contour in AIR method, demonstrated for the DMV 304HCu alloy at 20°C. For each threshold value, the corresponding contour area is computed; contours that flood the image are assigned an area of zero. The optimal threshold is identified as the first occurrence of a negative gradient in the area-threshold curve.

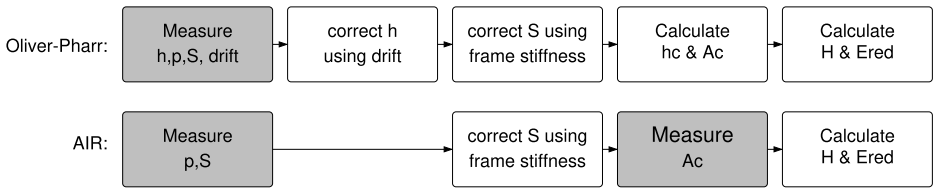


FIGURE 3 | Comparison of the O–P and AIR methods. Both methods measure the load (p) and stiffness (S), with the latter corrected for frame compliance. The O–P method additionally measures the indentation depth, corrects the depths for drift, and calculates the contact depth using the β-factor to determine the contact area. The AIR method, in contrast, directly measures the contact area via microscopy. Both approaches yield the reduced modulus (E_{red}) and hardness (H). Steps involving instrumentation are highlighted in dark gray.

15272648, 0, Downloaded from https://advanced.onlinelibrary.wiley.com/doi/10.1002/adem.202503193 by Universitatsbibliothek RWTH Aachen University, Wiley Online Library on [23/04/2026]. See the Terms and Conditions (https://onlinelibrary.wiley.com/terms-and-conditions) on Wiley Online Library for rules of use; OA articles are governed by the applicable Creative Commons License

corresponding to the transition from valid to invalid contour detection (see Figure 4).

e. The final contact area, A_c, was computed from the selected contour area (in pixels) using the microscope pixel size (1 pixel = 0.1264 µm).

The hardness, H, was calculated from the maximum applied force, P_{max}, and the contact area determined via the AIR workflow:

$$H = \frac{P_{max}}{A_c} \tag{3}$$

Because the measured compliance includes both frame and contact compliance, the reduced modulus, E_r, was determined as [14, 17]

$$E_r = \sqrt{\frac{\pi}{4A_c}}\left(\frac{1}{C_{measure} - C_{frame}}\right) \tag{4}$$

The specimen elastic modulus, E, was subsequently calculated from E_r using the known elastic modulus and Poisson's ratio of the cBN nanoindenter tip, i.e., E_{tip} = 800 GPa and ν_{tip} = 0.12, respectively.

To quantify the influence of individual chemical elements on alloy hardness, we combined exploratory and inferential statistical approaches. Pairwise correlation coefficients were visualized as heatmaps using the Seaborn library (v0.12.2) [23] to examine composition–property relationships. Statistical significance was evaluated through hypothesis testing implemented in the statsmodels library (v0.13.5) [24]), where p-values were computed to evaluate the association between elemental concentration and hardness. The null hypothesis assumed no association; smaller p-values therefore indicate stronger evidence against this assumption. Finally, iterative backward elimination—sequentially removing variables with the highest p-values—was applied to identify the subset of elements most strongly and significantly correlated with hardness.

3 | Results

Seven alloys were investigated to span a wide range of crystal structures and chemical compositions. The set comprises three ferritic steels (16Mo3, 13CrMo4-5, and 10CrMo9-10), one martensitic steel (T91; X10CrMoVNb9-1), two austenitic steels (DMV 304HCu; X6CrNi18-10 and Sanicro 25; X1NiCrMoCuN31-27-4), and one nickel-based alloy (Alloy 617; NiCr23Co12M), as summarized in Table 1.

3.1 | Hardness as a Function of Temperature

Figure 5 presents the temperature-dependent hardness obtained from single-cycle indentation curves analyzed using the O–P method. These measurements, obtained in two independent test series, are shown primarily for comparison, highlighting the impact of not applying sample-specific frame-compliance calibration. Measurements were performed in two independent test series. In the first series (Figure 5a), three ferritic steels and the martensitic steel T91 were examined. Among these materials, T91, which contains the highest Cr concentration, exhibited the highest hardness over the entire temperature range. In the second series (Figure 5b), T91 was included as a reference together with two austenitic steels and the Ni-based alloy 617, spanning increasing Ni content (Table 1). Alloy 617 (sample 7) displayed the highest hardness within this series and retained hardness more effectively at elevated temperatures than the martensitic T91. A comparison of T91 hardness values between the two test series (Figure 5b) reveals systematic offsets in absolute values at each temperature while preserving the overall temperature dependence. These offsets are attributed to the absence of frame-compliance calibration in single loading–unloading measurements, which limits quantitative comparability between independent test series.

To enable frame-compliance calibration, cyclic nanoindentation experiments were performed on all seven alloys. The cyclic loading results (Figure 6a) show a systematic decrease in hardness with increasing temperature, with the largest hardness reduction occurring between 400°C and 600°C.

Several alloys (10CrMo9-10, 13CrMo4-5, and Alloy 617) exhibit a hardness increase at 200°C and 400°C. As discussed below, this behavior coincides with elevated thermal drift and/or increased uncertainty in frame-compliance determination (Figure 2) and is therefore attributed to measurement artifacts. Accordingly, hardness values at intermediate temperatures should be interpreted

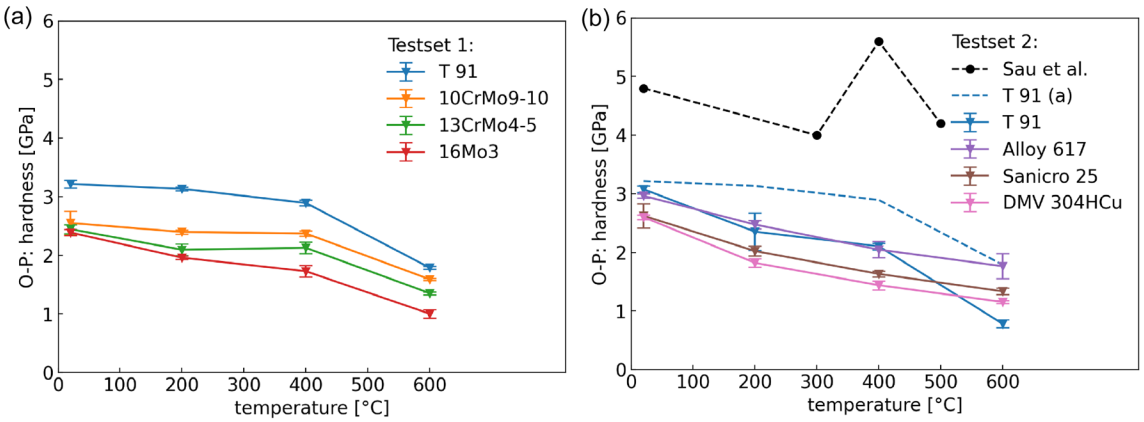


FIGURE 5 | Temperature-dependent hardness determined using the O–P method. Error bars represent the standard error of the mean (n = 6 independent nanoindentation curves per sample). (a) First series: ferritic and martensitic steels (see Table 1). (b) Second series: martensitic, austenitic, and Ni-based alloys. For reference, T91 data from panel (a) are reproduced in panel (b); literature data are included from [25].

15272648, 0, Downloaded from https://advanced.onlinelibrary.wiley.com/doi/10.1002/adem.202503193 by Universitatsbibliothek RWTH Aachen University, Wiley Online Library on [23/04/2026]. See the Terms and Conditions (https://onlinelibrary.wiley.com/terms-and-conditions) on Wiley Online Library for rules of use; OA articles are governed by the applicable Creative Commons License

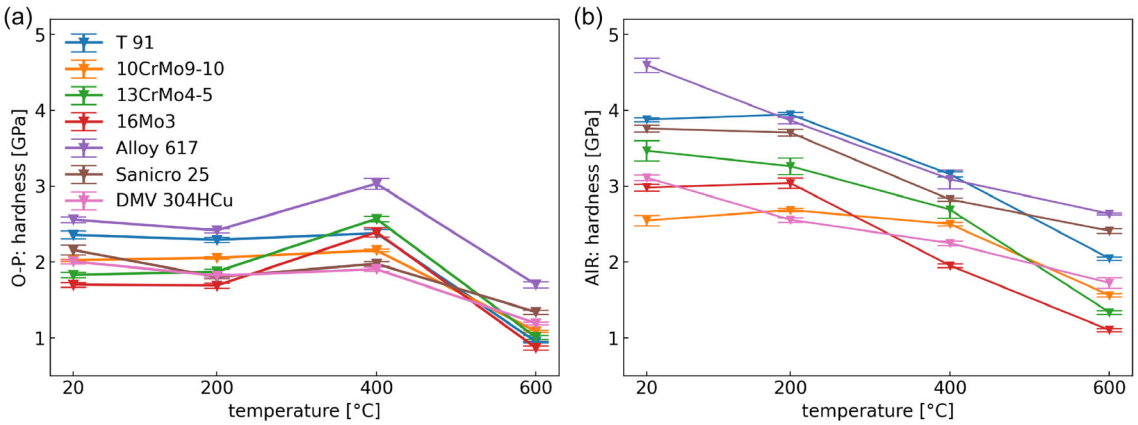


FIGURE 6 | Temperature-dependent hardness obtained from cyclic nanoindentation. Error bars represent the standard error calculated from eight independent indentations, each averaged over five loading–unloading cycles. (a) Hardness determined by the O–P method using frame-compliance correction. (b) Hardness determined using the AIR method.

with caution. Despite these uncertainties, all investigated materials demonstrate substantial mechanical stability (hardness decrease factor ~2) over the studied temperature range. It should be noted that the O–P method assumes the material exhibits sink-in behavior, requiring ad hoc corrections if visual inspection reveals a ductile behavior—for example, by switching the material class [26]. Such corrections increase the apparent contact area and, consequently, reduce the reported hardness. Since these manual adjustments affect all metals in a similar manner, i.e., shifting the curves consistently, they do not alter the relative ranking of the alloys.

3.2 | AIR-Based Hardness Determination and Imprint Quality

Hardness values determined using AIR are shown in Figure 6b. By directly measuring the residual imprint are, the AIR method avoids cumulative drift errors inherent to the depth-based analyses such as the O–P method. Consequently, AIR-derived hardness values exhibit a more nearly linear decrease with increasing temperature. The overall temperature dependence and relative ranking of the alloys are preserved: Alloy 617 and T91 are consistently the hardest materials, while 16Mo3 exhibits the lowest hardness.

Representative indentation imprints at 20°C are shown in Figure 7. Most imprints are symmetric and exhibit well-defined contact perimeters suitable for accurate area determination. However, two common sources of error are evident. First, slight sample tilt can produce asymmetric imprints (e.g., 16Mo3 and Alloy 617), introducing systematic bias in the extracted contact area. Second, surface defects—such as those observed for 10CrMo9-10, likely associated with a thin oxidation layer—disrupt the topographic signal and complicate contour detection. Similar effects may arise from scratches or inclusions, leading to spurious edge detection and erroneous area assignment.

3.3 | Thermal Drift

Thermal drift reflects the thermal stability of the nanoindenter system and manifests as apparent tip motion under constant load. Figure 8 summarizes the measured thermal-drift rates across all experiments.

At 20°C, drift fluctuated with a mean value of -0.56 ± 0.30 nm/s, indicating negligible systematic drift. At 200°C, intermittent positive drift spikes up to 2–3 nm/s were observed, although the mean value was much lower (1.14 ± 0.64 nm/s). Drift increased substantially at 400°C, reaching instantaneous rates of 6 nm/s and a mean value of 3.51 ± 0.90 nm/s. At 600°C, the drift magnitude decreased and stabilized within approximately -1 to 1 nm/s, with a mean of -0.82 ± 0.34 nm/s.

Although the O–P method includes a thermal-drift correction procedure [27], the large instantaneous drift rates observed at 200°C and 400°C exceed recommended limits and reduce the reliability of depth-based corrections.

3.4 | Frame Compliance

Frame compliance was evaluated from cyclic loading data acquired at multiple normal force levels (Figure 2a). According to the Sneddon relation and a series-spring approximation, compliance plotted against the inverse square root of

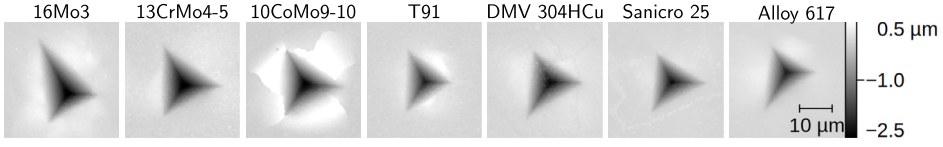


FIGURE 7 | Representative residual indentation imprints at 20°C. Most images show symmetric imprints with clearly defined contact perimeter suitable for AIR analysis. Examples of asymmetric imprints caused by sample tilt (16Mo3, Alloy 617) and surface-defect-induced contour disruption (10CoMo9-10) are highlighted.

15272648, 0, Downloaded from https://advanced.onlinelibrary.wiley.com/doi/10.1002/adem.202503193 by Universitatsbibliothek RWTH Aachen University, Wiley Online Library on [23/04/2026]. See the Terms and Conditions (https://onlinelibrary.wiley.com/terms-and-conditions) on Wiley Online Library for rules of use; OA articles are governed by the applicable Creative Commons License

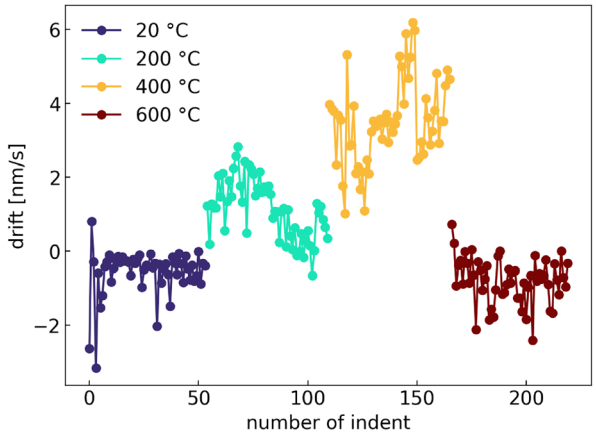


FIGURE 8 | Thermal-drift rates measured during nanoindentation experiments, color-coded by test temperature (dark blue = lowest temperature; dark red = highest temperature). Each indentation lasted approximately 1 min; extended equilibration periods were used between tests to minimize transient thermal effects.

load yields an intercept corresponding to the intrinsic frame compliance. Temperature-dependent variations in frame stiffness values (inverse compliance) are summarized in Figure 2b.

Data obtained at the lowest normal force (100 mN) systematically deviated from the regression line and were therefore excluded; a minimum force of 150 mN was deemed necessary for reliable contact establishment. Substantial scatter is observed, particularly at 600°C.

Mean frame stiffness values and associated uncertainties are reported in Table S1. The mean frame stiffness closely mirrors the drift rate shown in Figure 8 for all metals: it is low at 20°C and 200°C, increases at 400°C, and then decreases at 600°C. This variability spans roughly a factor of two across samples and temperatures. Additionally, the uncertainty in frame stiffness increases with temperature (see Table S1). At 20°C and 200°C, most samples exhibit errors between 5% and 10%. Only for 13CrMo4-5 and 10CrMo9-10 errors are below 5% at room temperature. At 400°C, 16Mo3 and 13CrMo4-5 exceed the 10% uncertainty, and at 600°C all samples show errors greater than 10%. This increasing uncertainty contributes directly to the scatter observed in depth-based hardness and modulus measurements.

Frame stiffness correlates with thermal drift but shows no systematic dependence on nominal test temperature (Figure 2b).

3.5 | Elastic Modulus

The determination of the elastic modulus by nanoindentation is strongly affected by fluctuations in frame stiffness and thermal drift. After correcting for these effects, the apparent elastic modulus obtained using the O–P method decreases with increasing temperature for all alloys (Figure 9a), consistent with literature expectations. However, at 600°C, all samples exhibit an anomalous increase in the apparent modulus, most pronounced for 10CoMo9-10 and 13CrMo4-5.

At 600°C, significant time-dependent creep was observed during indentation. Therefore, the power-law correction proposed by Ngan et al. [20] was applied. This correction is only valid when creep is present; applying it at lower temperatures yields nonphysical results.

Figure 9b shows the elastic moduli after applying the creep correction at 600°C. The corrected values are systematically reduced relative to the uncorrected data, restoring the expected monotonic decrease of elastic modulus with temperature for most alloys. Alloy 617 agrees well with reference data, although its modulus at 600°C remains higher than both the reference value and the value measured at 400°C.

4 | Discussion

Accurate interpretation of nanoindentation force–depth curves requires correction for thermal drift and instrument frame stiffness, as well as robust surface detection and calibration of the indenter tip area function; the latter corrections were not addressed in the present study. Correcting the penetration depth for thermal drift is particularly critical at elevated temperatures, as uncorrected drift introduces artifacts in the calculated contact area, contact depth, and unloading stiffness.

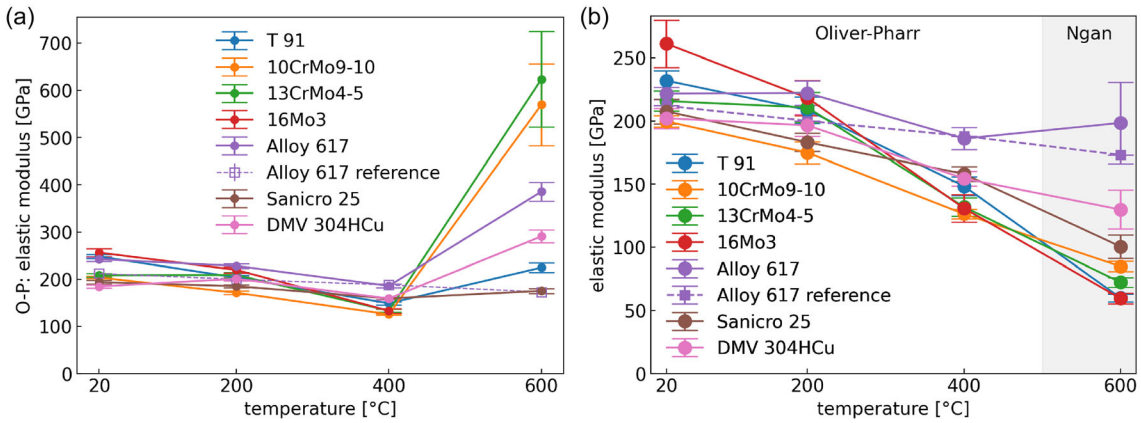


FIGURE 9 | Elastic modulus as a function of temperature: a) moduli determined using the O–P method; values at 600°C are unphysically high due to creep. b) Same data after applying the power-law correction of Ngan et al. [20] at 600°C. Error bars denote the standard error ($n = 8$ indentations, five cycles per indentation).

15272648, 0, Downloaded from https://advanced.onlinelibrary.wiley.com/doi/10.1002/adem.202503193 by Universitatsbibliothek RWTH Aachen University, Wiley Online Library on [23/04/2026]. See the Terms and Conditions (https://onlinelibrary.wiley.com/terms-and-conditions) on Wiley Online Library for rules of use; OA articles are governed by the applicable Creative Commons License

4.1 | Quantification of Temperature-Dependent Measurement Challenges

Thermal drift arises from temperature gradients and differential thermal expansion between the indenter tip and the sample. These gradients typically increase with heating rate but decrease with prolonged thermal stabilization. In standard practice, the drift rate is estimated by monitoring the indenter displacement under a small, constant normal force immediately after unloading from the maximum load. This single drift rate is then extrapolated to the entire indentation cycle, implicitly assuming time- and condition-invariant drift behavior.

As shown in Figure 7, the measured drift rate varies substantially even at a fixed nominal temperature, indicating that conventional post-test drift correction provides only a coarse approximation and may not reflect the instantaneous thermal drift experienced during indentation. The thermal equilibration time required to achieve stable conditions depends strongly on instrument geometry, temperature set-point, component thermal conductivities, and the efficiency of the water-cooling system [3]. Quantifying the true thermal stability of the nanoindenter is challenging because the proportional–integral–derivative (PID) control loop regulates temperature only at sensors adjacent to the heaters. Assessing spatial and temporal temperature homogeneity throughout the instrument would require additional distributed sensors, particularly in the most temperature-sensitive components, which are not currently instrumented.

In the present work, the extended stabilization interval applied prior to the 600°C experiments likely contributed to the reduced drift observed at that temperature, whereas the stabilization times used before the 200°C and 400°C tests appear to have been insufficient. Based on these observations, we recommend a thermal stabilization period of at least 2 h after reaching the target temperature before initiating indentation measurements when using the Micromaterials NanoXtreme instrument.

4.2 | Frame Stiffness and Its Interaction with Thermal Drift

Precise calibration of frame stiffness is essential for accurate determination of the elastic modulus, as the unloading stiffness depends directly on the stiffness of the instrument frame. Frame stiffness comprises contributions from the gantry, sample, tip mounting, and sample mounting, excluding only the tip–sample contact stiffness. Typically, frame stiffness is calibrated by performing indentations at varying depths or loads on reference materials with constant elastic modulus [28]. The samples exhibited approximately constant elastic moduli, allowing us to verify that the order of magnitude of frame stiffness is consistent with typical nanoindentation values (approximately 1 MN/m), despite notable variability in the reported data. Importantly, a correlation was observed between the measured drift rates and the apparent frame stiffness, underscoring the interdependence of these quantities and the necessity of correcting thermal artifacts in nanoindentation data.

As summarized in Table S1, the uncertainty in frame stiffness increases systematically with temperature, reaching approximately 15% at 600°C for all investigated materials. Although modest differences between alloys are observed—10CrMo4-5, Sanicro 25, and Alloy 617 exhibit the lowest mean uncertainty—these differences are small relative to the dominant influence of temperature.

Thermal drift affects the apparent indentation depth, and because the calculated stiffness (or inverse compliance) depends on depth, an analytical relationship exists between thermal drift and frame stiffness. This relationship was quantified by analyzing the 6-s unloading segment, during which drift-induced changes in apparent depth were extracted from the force–depth curves and then propagated through the stiffness calculation. At 400°C, this interval corresponds to an artificial depth change of approximately 0.006 μm (Figure 8). Compared with the typical difference between maximum and contact depth (0.14 ± 0.05 μm), this contribution is modest (approximately 4.3%) and substantially smaller than the largest stiffness variations shown in Figure 2b. Moreover, thermal drift may act in either direction, producing either apparent increases or decreases in depth, although it appears predominantly unidirectional in the present dataset. Consequently, while thermal drift contributes to the observed evolution of frame stiffness, it cannot fully explain the large scatter in stiffness values.

4.3 | Elastic Modulus and Creep-Induced Artifacts

The anomalous behavior observed in the elastic modulus at 600°C (see Figure 9) is attributed to measurement artifacts associated with thermally activated creep during nanoindentation. Continued deformation during unloading causes additional penetration as the applied normal force decreases, artificially increasing the extracted contact stiffness and, in extreme cases, producing an apparent negative stiffness. Both effects lead to an overestimation of the elastic modulus and represent well-documented limitations of the O–P method when creep corrections are not applied [20, 29].

As shown in Figure 9a, the elastic modulus decreases monotonically with increasing temperature for all samples except at 600°C, where the O–P analysis yields an anomalous increase for every alloy. This effect is particularly pronounced for 10CoMo9-10 and 13CrMo4-5. Given the pronounced creep at high temperature and the substantial uncertainty in frame compliance, application of the creep correction proposed by Ngan et al. [20] is warranted.

Application of the Ngan creep correction yields reduced elastic moduli that agree more closely with manufacturer datasheet values than uncorrected measurements. However, applying this correction to datasets that do not exhibit measurable creep—specifically, those in which penetration depth does not increase during unloading—results in unphysical moduli. The Ngan correction should therefore be applied only when creep is demonstrably present.

Values for Young's modulus determined using the AIR method exhibit substantial scatter (Figure S1), making them currently unsuitable for practical applications. Further refinement of the contact area determination is needed before the AIR method can reliably determine Young's modulus.

4.4 | Hardness Measurement Challenges and Comparison of Analysis Methods

For T91, we observe a monotonic decrease in hardness with increasing temperature (Figure 5), in contrast to the

15272648, 0, Downloaded from https://advanced.onlinelibrary.wiley.com/doi/10.1002/adem.202503193 by Universitatsbibliothek RWTH Aachen University, Wiley Online Library on [23/04/2026]. See the Terms and Conditions (https://onlinelibrary.wiley.com/terms-and-conditions) on Wiley Online Library for rules of use; OA articles are governed by the applicable Creative Commons License

nonmonotonic trend reported by Sau et al. [25]. They attributed the hardness increase at 400°C to a limited sampling area that may not have captured a representative microstructural volume. Differences in sample preparation, testing parameters, and data analysis procedures may also contribute to this discrepancy, underscoring the experimental challenges inherent to high-temperature nanoindentation.

Thermal drift and frame compliance systematically bias mechanical properties derived using the O–P method. As shown in Figure 7, the AIR approach introduces a distinct set artifacts. Unlike O–P analysis, AIR determines the contact area directly from indentation images and is thus insensitive to thermal drift affecting force–depth data. Consequently, AIR-derived hardness values (Figure 6b) exhibit a more consistent linear temperature dependence than those obtained via the O–P analysis (Figure 6a), which show greater scatter. Nevertheless, AIR is susceptible to its own error modes (Figure 6), including:

- Sample tilt (Figure 7, samples 1 and 7), producing asymmetric indentation imprints that bias contact-area estimation.
- Surface defects such as oxidation layers (Figure 7, sample 3), which impede reliable contour extraction.

These artifacts can be mitigated through improved sample alignment, surface preparation, and more robust image processing algorithms.

Overall, the O–P and AIR approaches are affected by different systematic errors and should be employed as complementary techniques. Their combined use enhances measurement reliability and facilitates identification and quantification of method-specific limitations.

Beyond thermal drift and frame compliance, temperature-induced tip wear and material creep can introduce further artifacts. In principle, repeated tip-area calibrations on fused silica before and after each high-temperature experiment would quantify temperature-induced tip wear. In practice, this approach is impractical because it requires prolonged high-temperature exposure and relies on calibration standards that remain valid across a wide temperature range. Therefore, we employed the initial room-temperature tip calibration as the area function for all O–P analyses.

4.5 | Dependence of Mechanical Properties on Chemical Composition and Crystal Structure

We treat the composition–property comparisons as an exploratory, artifact-aware evaluation rather than as a mechanistic investigation. The primary objective is to determine whether, after (i) quantifying and correcting for instrument-related artifacts (thermal drift, frame compliance variations, and creep where present) and (ii) applying a complementary image-based area measurement (AIR), statistically meaningful correlations between alloy composition and indentation response can be resolved. We did not perform detailed microstructural or phase-transformation characterization (e.g., in situ diffraction, EBSD, or TEM); therefore, interpretations concerning phase transformations, precipitate evolution, or specific deformation mechanisms lie beyond the evidentiary scope of this study.

When assessing the temperature-dependent hardness, chemical composition and crystal structure must be considered jointly. Chemical composition governs hardness and high-temperature performance through mechanisms such as solid-solution strengthening, precipitation, and phase stability [30]. Crystal structure determines the dominant deformation mechanisms (e.g., available slip systems and twinning) and thus fundamentally controls mechanical response [31]. The interaction between composition and structure further modulates hardness.

Figure 10 reveals distinct relationships between alloying-element content (Cr, Ni) and hardness. In the ferritic steels 16Mo3, 13CrMo4-5, and 10CrMo9-10, as well as in the martensitic steel T91, increasing Cr content correlates with an approximately linear increase in hardness. By contrast, in DMV 304HCu, Sanicro 25, and Alloy 617, the hardness is more strongly influenced by the Ni concentration. These trends are broadly consistent with the literature reports, although direct quantitative comparisons are limited by differences in base composition, microstructure, phase constitution, thermomechanical processing, and characterization methods. Li et al. [32] demonstrated a pronounced

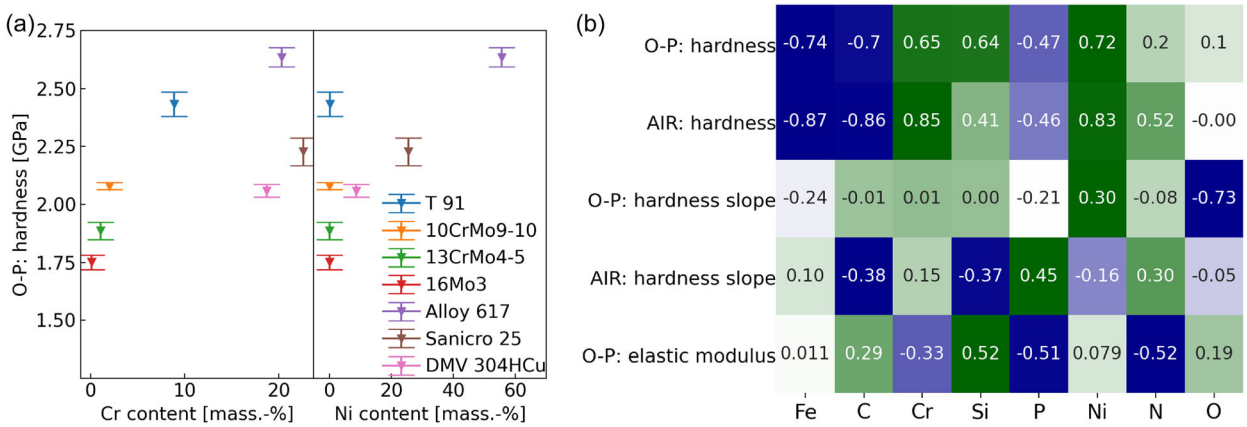


FIGURE 10 | Evolution of hardness as a function of alloy chemical composition (Table 1). (a) Hardness measured at 20°C plotted as a function of Cr content (wt%) and Ni content (wt%). (b) Heatmap illustrating absolute hardness and the temperature sensitivity of hardness (slope dH/dT) obtained using two analysis methods: O–P and AIR. The results indicate a positive correlation between hardness and the contents of Cr, Si, and Ni in the investigated alloys.

15272648, 0, Downloaded from https://advanced.onlinelibrary.wiley.com/doi/10.1002/adem.202503193 by Universitatsbibliothek RWTH Aachen University, Wiley Online Library on [23/04/2026]. See the Terms and Conditions (https://onlinelibrary.wiley.com/terms-and-conditions) on Wiley Online Library for rules of use; OA articles are governed by the applicable Creative Commons License

hardening effect of Cr in steel-bonded carbide alloys. Ahssi et al. [33] reported that Ni additions up to 13% increased yield strength and hardness in Nb–V microalloyed powder-metallurgy steels, whereas higher Ni contents reduced strength while increasing elongation. Similarly, Demirtas and Erden [34] found that Cr and Ni additions improved the mechanical properties of plain carbon steel up to 1 wt%, beyond which properties declined; that reduction was attributed to the powder-metallurgy processing route.

Figure 10d presents a heatmap quantifying the contribution of individual alloying elements to hardness, as determined by the O–P and AIR methods. Hardness values were taken from O–P measurements at 20°C and from AIR measurements at 600°C, as these temperatures resulted in the lowest scatter of the respective methods. The heatmap also characterizes the relationship between chemical composition and the temperature dependence of hardness, expressed as the slope of hardness versus temperature. Cells with values approaching +1 (dark green) or −1 (dark blue) indicate strong positive or negative influences, respectively, whereas white cells denote negligible effects. The hardness maps obtained by the two methods show good agreement: Ni, Cr, and Si exhibit positive correlations with hardness, consistent with previous studies [33, 35, 36], while Fe and C display inverse correlations.

To identify the elements most strongly associated with degradation of mechanical properties at elevated temperature, the slope of hardness versus temperature was quantified by linear regression of across the full dataset. Heatmaps of this slope derived from the O–P and AIR analyses show poor agreement. The O–P heatmap indicates that Ni and O are associated with an increased rate of hardness reduction with temperature, consistent with earlier reports linking oxygen content to hardness degradation [33, 37]. By contrast, the AIR method suggests correlations between the hardness–temperature slope and C, Si, and P, relationships that have not, to our knowledge, been reported previously. For the present dataset, the O–P analysis therefore yields trends that align more closely with published observations than those obtained using AIR.

Evaluating hardness slopes over the full temperature range is inherently challenging. Slope estimates generally carry greater uncertainty than point measurements because experimental errors propagate and accumulate during gradient determination. As a result, comparisons of hardness at a single, well-defined temperature are more reliable and statistically robust than comparisons based on slope values.

The final row of Figure 10b highlights the influence of chemical composition on the elastic modulus using the O–P method. Cr, C, and P exhibit particularly strong correlations with the elastic modulus. It should be noted that in many cases, the elastic modulus could not be extracted using the AIR method because the term $C_{\mathrm{measure}}-C_{\mathrm{frame}}$ in Equation (4) became negative, which is physically implausible. These negative compliances are attributed to measurement artifacts caused by pronounced thermal drift during high-temperature testing.

Elements showing the strongest correlations with hardness in both the O–P and AIR analyses were selected as candidate predictors for subsequent statistical evaluation. In the first step, *p*-values describing the associations between hardness and the concentrations of Fe, C, Cr, Si, and Ni were calculated (Table 2). A backward-elimination procedure was then applied: at each iteration, the element with the highest *p*-value was removed and the analysis repeated. The process terminated when only Fe, Cr, and Ni remained, as their *p*-values converged to similar values (approximately 0.3) in the third iteration.

Although *p*-values below a conventional significance threshold of 0.05 are typically interpreted as evidence of statistically significant correlations (see Section 2), achieving such thresholds is challenging for high-temperature indentation data. The experimental context involves potential nonlinear relationships and additional sources of uncertainty—such as crystallographic orientation effects and measurement noise—that reduce the statistical power of linear hypothesis tests. Within these limitations, the present analysis indicates that, in addition to the primary role of Fe in steels, the Cr and Ni concentrations are relevant contributors to the observed hardness trends (see Figure 10a and the *p*-value analysis).

It is noteworthy that Si was eliminated in the first backward-elimination step despite its well-established role in impeding plastic deformation and increasing hardness. This apparent discrepancy likely reflects limited variation in Si content across the alloy set (Si contents were similar in all but one alloy), which reduces the statistical sensitivity to detect its influence, as well as potential measurement artifacts.

Beyond chemical composition, mechanical properties are strongly governed by the crystal structure [33]. For example, the comparatively high hardness of martensitic T91 is consistent with expectations [38] for martensitic steels containing strengthening precipitates; however, direct confirmation of precipitate state or transformation behavior in the tested specimens was not undertaken here. Prior studies [39] have shown that in-service microstructural evolution (e.g., precipitate coarsening or compositional redistribution) can significantly modify mechanical response. Therefore, although the nominal BCC structure of T91 may be retained after long service periods, its mechanical behavior can change substantially.

By contrast, the austenitic alloys exhibit lower hardness at ambient temperature and, in some high-temperature tests, comparatively reduced softening. These trends are qualitatively consistent with typical FCC behavior. Mechanistic interpretations of such FCC responses (such as thermally activated slip processes) have

TABLE 2 | Analysis of *p*-values describing the correlation between individual chemical elements and material hardness at 20°C according to the O–P method across three iterations of backward elimination. In each iteration, the element with the highest *p*-value (indicating the weakest evidence against the null hypothesis of no correlation) is highlighted in italic and removed prior to the subsequent iteration. Elements retained after the final iteration therefore exhibit the strongest statistical association with hardness.

	First step	Second step	Third step
Fe	0.624	0.121	0.281
C	0.603	*0.196*	—
Cr	0.644	0.123	0.294
Si	*0.909*	—	—
Ni	0.619	0.123	0.289

15272648, 0, Downloaded from https://advanced.onlinelibrary.wiley.com/doi/10.1002/adem.202503193 by Universitatsbibliothek RWTH Aachen University, Wiley Online Library on [23/04/2026]. See the Terms and Conditions (https://onlinelibrary.wiley.com/terms-and-conditions) on Wiley Online Library for rules of use; OA articles are governed by the applicable Creative Commons License

been established in the literature through microstructural evidence (e.g., by Weinberger et al. [40] and Sanders et al. [41]), but no such direct mechanistic validation is presented here. Overall, the relative ranking of the seven materials is consistent with the nanoindentation hardness measured at 20°C using the O–P method—where thermal drift was negligible—and with the hardness obtained by AIR at 600°C—where image-recognition errors were minimized—as shown in Figure 5.

5 | Conclusions

This study pursued two primary objectives in high-temperature nanoindentation: (1) to characterize methodological and temperature-induced measurement challenges, and (2) to evaluate how alloy composition influences hardness as a function of temperature.

Thermal effects manifested as both drift and temperature-dependent fluctuations in frame stiffness. Although extended stabilization periods reduced thermal drift, they did not fully suppress frame-stiffness variability at elevated temperatures.

The O–P and AIR analysis approaches proved complementary. The O–P method provides higher accuracy at lower temperatures but is more sensitive to thermal artifacts. Consequently, the AIR method offers advantages for hardness measurements under conditions where such artifacts are dominant.

All alloys exhibited systematic hardness degradation with increasing temperature. Ngan's correction to the O–P method is valid only when appreciable creep is present—a condition satisfied here only at 600°C. Applying Ngan's correction at that temperature reduced the measured elastic modulus to values consistent with literature reports.

Despite substantial scatter in the mechanical-property data, the combination of heat-map visualization and statistical (p-value) analyses enabled extraction of meaningful materials-science trends: both chromium and nickel additions strengthened the alloys and improved hardness retention with increasing temperature.

The present work is subject to several limitations: First, the tip area function was calibrated at room temperature only; therefore, potential temperature-dependent changes in contact area are not explicitly quantified. Second, several sources of uncertainty are nonstationary and partially correlated, including time-dependent thermal drift, temperature nonuniformity across the sample holder, and changes in frame stiffness. Third, although the major contributors to measurement uncertainty are assessed individually, a single, fully propagated uncertainty budget is not constructed. Fourth, AIR-based contour detection may fail or become biased for imprints affected by surface defects, oxidation layers, or significant sample tilt.

A key methodological priority moving forward is the development of predictive approaches for thermal drift, rather than relying solely on post hoc extrapolation. Fluctuations in thermal drift represent a principal obstacle to reliable determination of mechanical properties, particularly in high-temperature nanoindentation, and improved modeling or control strategies would substantially enhance measurement robustness.

Acknowledgements

Open Access funding enabled and organized by Projekt DEAL.

Conflicts of Interest

The authors declare no conflicts of interest.

Data Availability Statement

The data that support the findings of this study are available from the corresponding author upon reasonable request.

References

1. W. C. Oliver and G. M. Pharr, "An Improved Technique for Determining Hardness and Elastic Modulus Using Load and Displacement Sensing Indentation Experiments," *Journal of Materials Research* 7, no. 6 (1992): 1564–1583, ISSN 0884-2914, 2044-5326, https://doi.org/10.1557/JMR.1992.1564.

2. E. Özçelikci, H. İlcan, G. Yıldırım, and M. Şahmaran, "11 - Nanoscale Characterization of Cementitious Composites," *Recent Advances in Nano-Tailored Multi-Functional Cementitious Composites, Woodhead Publishing Series in Civil and Structural Engineering*, eds. M. Şahmaran, F. Shaikh and G. Yıldırım, (Woodhead Publishing, 2022), pp. 375–406, https://doi.org/URL-10.1016/B978-0-323-85229-6.00006-8, https://www.sciencedirect.com/science/article/pii/B9780323852296000068.

3. J. M. Wheeler, D. E. J. Armstrong, W. Heinz, and R. Schwaiger, "High Temperature Nanoindentation: The State of the Art and Future Challenges," *Current Opinion in Solid State and Materials Science* 19, no. 6 (2015): 354–356, ISSN 13590286, https://doi.org/10.1016/j.cossms.2015.02.002.

4. A. Dey, S. Mandal, S. Bhandari, C. Pal, J. T. Orasugh, and D. Chattopadhyay, "Chapter 2 - Characterization Methods. In Baoguo Han, Sumit Sharma, Tuan Anh Nguyen, Li Longbiao," *Fiber-Reinforced Nanocomposites: Fundamentals and Applications, Micro and Nano Technologies*, Eds. K. S. Bhat, (Elsevier, 2020), pp. 7–67, https://doi.org/URL-10.1016/B978-0-12-819904-6.00002-5, https://www.sciencedirect.com/science/article/pii/B9780128199046000025.

5. B. D. Beake, and J. F. Smith, "High-Temperature Nanoindentation Testing of Fused Silica and Other Materials," *Philosophical Magazine A* 82, no. 10 (2002): 2179–2186, https://doi.org/10.1080/01418610208235727.

6. C. A. Schuh, C. E. Packard, and A. C. Lund, "Nanoindentation and Contact-Mode Imaging at High Temperatures," *Journal of Materials Research* 21, no. 3 (2006): 725–0736, ISSN 0884-2914, 2044-5326, https://doi.org/10.1557/jmr.2006.0080.

7. Z. C. Duan, and A. M. Hodge, "High-Temperature Nanoindentation: New Developments and Ongoing Challenges," *JOM* 61, no. 12 (2009): 32–36, ISSN 1047-4838, 1543-1851, https://doi.org/10.1007/s11837-009-0177-5.

8. J. C. Trenkle, C. E. Packard, and C. A. Schuh, "Hot Nanoindentation in Inert Environments," *Review of Scientific Instruments* 81, no. 7 (2010): 073901, ISSN 0034-6748, https://doi.org/10.1063/1.3436633.

9. J. M. Wheeler and J. Michler, "*Invited Article: Indenter materials for high temperature nanoindentation*," 84, no. 10 (2013): 101301, ISSN 0034-6748, 1089-7623, https://doi.org/10.1063/1.4824710.

10. S. Verma, P. Sarkar, and P. Pant, "Thermal Drift in Room Temperature Nanoindentation Experiments: Measurement and Correction," *Journal of Materials Research* 36, no. 17 (2021): 3436–3444, https://doi.org/10.1557/s43578-021-00386-0.

11. M. Schmahl, C. Müller, R. Meinke, E. G. Alves Alcantara, U. D. Hangen, and C. Fleck, "Cyclic Nanoindentation for Local High

15272648, 0, Downloaded from https://advanced.onlinelibrary.wiley.com/doi/10.1002/adem.202503193 by Universitatsbibliothek RWTH Aachen University, Wiley Online Library on [23/04/2026]. See the Terms and Conditions (https://onlinelibrary.wiley.com/terms-and-conditions) on Wiley Online Library for rules of use; OA articles are governed by the applicable Creative Commons License

Cycle Fatigue Investigations: A Methodological Approach Accounting for Thermal Drift," *Advanced Engineering Materials* 25 (2023): e202201676, https://doi.org/10.1002/adem.202201676.

12. J. Nohava, N. X. Randall, and N. Conté, "Novel Ultra Nanoindentation Method with Extremely Low Thermal Drift: Principle and Experimental Results," *Journal of Materials Research* 24, no. 3 (2009): 873–882, https://doi.org/10.1557/jmr.2009.0114, https://www.cambridge.org/core/journals/journal-of-materials-research/article/novel-ultra-nanoindentation-method-with-extremely-low-thermal-drift-principle-and-experimental-results/6A0B9AFD6CE06B2D55CBA0187322FB88.

13. M. Conte, G. Mohanty, J. J. Schwiedrzik, et al., "Novel High Temperature Vacuum Nanoindentation System with Active Surface Referencing and Non-Contact Heating for Measurements up to 800 °c," *Review of Scientific Instruments* 90, no. 4 (2019): 045105, https://doi.org/10.1063/1.5029873.

14. S. Brinckmann, and R. Schwaiger, "Towards Enhanced Nanoindentation by Image Recognition," *Journal of Materials Research* 36, no. 11 (2021): 2266–2276, ISSN 0884-2914, 2044-5326, https://doi.org/10.1557/s43578-021-00173-x.

15. S. Wang, and H. Zhao, "Low Temperature Nanoindentation: Development and Applications," *Micromachines* 11, no. 4 (2020): 407.

16. J. Svidró, A. Diószegi, and J. T. Svidró, "The Origin of Thermal Expansion Differences in Various Size Fractions of Silica Sand," *International Journal of Cast Metals Research* 33, no. 6 (2020): 242–249, https://doi.org/10.1080/13640461.2020.1838078.

17. I. N. Sneddon, "The relation between load and penetration in the axisymmetric boussinesq problem for a punch of arbitrary profile," *International Journal of Engineering Science* 3, no. 1 (1965): 47–57, ISSN 00207225, https://doi.org/10.1016/0020-7225(65)90019-4.

18. K. I. Schiffmann, "Area Function Calibration in Nanoindentation Using the Hardness Instead of Young's Modulus of Fused Silica as a Reference Value," *International Journal of Materials Research* 98, no. 5 (2007): 424–429, ISSN 2195-8556, 1862-5282, https://doi.org/10.3139/146.101488.

19. C. R. Harris, K. J. Millman, S. J. van der Walt, et al., "Array Programming with NumPy," *Nature* 585, no. 7825 (2020): 357–362, ISSN 0028-0836, 1476-4687, https://doi.org/10.1038/s41586-020-2649-2.

20. A. H. W. Ngan, H. T. Wang, B. Tang, and K. Y. Sze, "Correcting Power-Law Viscoelastic Effects in Elastic Modulus Measurement Using Depth-Sensing Indentation," *International Journal of Solids and Structures* 42, no. 5-6 (2005): 1831–1846, ISSN 00207683, https://doi.org/10.1016/j.ijsolstr.2004.07.018.

21. D. Nečas, and P. Klapetek, "Gwyddion: an Open-Source Software for SPM Data Analysis," *Open Physics* 10, no. 1 (2012): 181–188, ISSN 2391-5471, https://doi.org/10.2478/s11534-011-0096-2.

22. G. Bradski, "The OpenCV Library," *Dr. Dobb's Journal of Software Tools* 3 (2000): 1–81.

23. M. Waskom, "Seaborn: Statistical Data Visualization," *Journal of Open Source Software* 6, no. 60 (2021): 3021, ISSN 2475-9066, https://doi.org/10.21105/joss.03021.

24. J. S. Seabold and J. Perktold, "Statsmodels: Econometric and Statistical Modeling with Python," *Proceedings of the 9th Python in Science Conference*, (2010).

25. M. Sau, E. D. Hintsala, Y. Chen, et al., "High-Throughput Nanoindentation Mapping of Additively Manufactured T91 Steel," *JOM* 74, no. 4 (2022): 1469–1476, ISSN 1047-4838, 1543-1851, https://doi.org/10.1007/s11837-022-05189-0.

26. KLA, *Nano Indenter G200X User and Service Manual*, 2019.

27. Agilent, *Nano Indenter G200: User's Guide*, 2013.

28. Keysight, Rapid Calibration of Area Function and Frame Stiffness with Express Test, ISSN Application Note 5991-1453EN, 2014.

29. G. Feng and A. H. W. Ngan, "Effects of Creep and Thermal Drift on Modulus Measurement Using Depth-Sensing Indentation," *Journal of Materials Research* 17, no. 3 (2002): 660–668, ISSN 0884-2914, 2044-5326, https://doi.org/10.1557/JMR.2002.0094.

30. M. A. Suárez, R. Esquivel, J. Alcántara, H. Dorantes, and J. F. Chávez, "Effect of Chemical Composition on the Microstructure and Hardness of Al–Cu–Fe Alloy," *Materials Characterization* 62, no. 9 (2011): 917–923, ISSN 10445803, https://doi.org/10.1016/j.matchar.2011.06.009.

31. W. Chubb, "Contribution of Crystal Structure to the Hardness of Metals," *JOM* 7, no. 1 (1955): 189–192, ISSN 1047-4838, 1543-1851, https://doi.org/10.1007/BF03377478.

32. G. Li, W. Chen, N. Wu, Y. Lyu, L. Guo, and F. Luo, "Effect of Cr content and its alloying method on microstructure and mechanical properties of high-manganese steel-bonded carbide," 101 (2021): 105698, ISSN 02634368, https://doi.org/10.1016/j.ijrmhm.2021.105698.

33. M. A. M. Ahssi, M. A. Erden, M. Acarer, and H. Çuğ, "Mehmet Akif Erden, Mustafa Acarer, and Harun Çuğ," *Materials* 13, no. 18 (2020): 4021, ISSN 1996-1944, https://doi.org/10.3390/ma13184021.

34. H. Demirtaş, and M. A. Erden, "Cr ve Ni İlavesinin Sade Karbonlu Çeliğin Mekanik Özelliklerine Etkisi," *Duzce University Journal of Science and Technology* 7, no. 3 (2019): 1217–1223, ISSN 2148-2446, https://doi.org/10.29130/dubited.539930.

35. T. M. Ribeiro, E. Catellan, A. Garcia, and C. A. dos Santos, "The effects of Cr addition on microstructure, hardness and tensile properties of as-cast Al–3.8wt.%Cu–(Cr) alloys," *Journal of Materials Research and Technology* 9, no. 3 (2020): 6620–6631, ISSN 22387854, https://doi.org/10.1016/j.jmrt.2020.04.054.

36. J. Liu, W. Liu, Z. Hao, et al., "Effects of Silicon Content and Tempering Temperature on the Microstructural Evolution and Mechanical Properties of HT-9 Steels," *Materials* 13, no. 4 (2020): 972, ISSN 1996-1944, https://doi.org/10.3390/ma13040972.

37. C. Catanio Bortolan, L. Contri Campanelli, C. Paternoster, et al., "Effect of oxygen content on the mechanical properties and plastic deformation mechanisms in the TWIP/TRIP Ti–12Mo alloy," *Materials Science and Engineering: A* 817 (2021): 141346, ISSN 09215093, https://doi.org/10.1016/j.msea.2021.141346.

38. M. Ogura, T. Fukushima, R. Zeller, and P. H. Dederichs, "Structure of the high-entropy alloy Al CrFeCoNi: fcc versus bcc," *Journal of Alloys and Compounds* 715 (2017): 454–459, ISSN 09258388, https://doi.org/10.1016/j.jallcom.2017.04.318.

39. Y. Li, J. Du, L. Li, K. Gao, X. Pang, and A. A. Volinsky, "Mechanical properties and phases evolution in T91 steel during long-term high-temperature exposure," *Engineering Failure Analysis* 111 (2020): 104451, ISSN 13506307, https://doi.org/10.1016/j.engfailanal.2020.104451.

40. C. R. Weinberger, B. L. Boyce, and C. C. Battaile, "Slip Planes in Bcc Transition Metals," *International Materials Reviews* 58, no. 5 (2013): 296–314, ISSN 0950-6608, https://doi.org/10.1179/1743280412Y.0000000015.

41. W. S. Sanders and L. J. Gibson, "Mechanics of BCC and FCC hollow-sphere foams," *Materials Science and Engineering: A* 352, no. 1-2 (2003): 150–161, ISSN 09215093, https://doi.org/10.1016/S0921-5093(02)00890-0.

Supporting Information

Additional supporting information can be found online in the Supporting Information section. **Supporting Fig. S1:** Elastic modulus as a function of the temperature according to the AIR analysis. The moduli scatter more than the values according to the Oliver-Pharr method. **Supporting Table S1:** Frame compliance error using high temperature nanoindentation for the seven samples. The test protocol involved cyclic loading-unloading profile at maximum normal force 500 mN with 5 cycles, 5 s loading, 5 s unloading and 5 s holding time for each cycle. Frame compliance error color coding: green-less than 5%, yellow-between 5% and 10%, red-above 10%.

15272648, 0, Downloaded from https://advanced.onlinelibrary.wiley.com/doi/10.1002/adem.202503193 by Universitatsbibliothek RWTH Aachen University, Wiley Online Library on [23/04/2026]. See the Terms and Conditions (https://onlinelibrary.wiley.com/terms-and-conditions) on Wiley Online Library for rules of use; OA articles are governed by the applicable Creative Commons License